

# DAAF: Degradation-Aware Adaptive Fusion Framework for Robust Infrared and Visible Images Fusion

Tianpei Zhang, Jufeng Zhao, Yiming Zhu, Guangmang Cui, Yuxin Jing, Yuhan Lyu

**Abstract**—Existing infrared and visible image fusion (IVIF) algorithms often prioritize high-quality images, neglecting image degradation such as low light and noise, which limits the practical potential. This paper propose Degradation-Aware Adaptive image Fusion (DAAF), which achieves unified modeling of adaptive degradation optimization and image fusion. Specifically, DAAF comprises an auxiliary Adaptive Degradation Optimization Network (ADON) and a Feature Interactive Local-Global Fusion (FILGF) Network. Firstly, ADON includes infrared and visible-light branches. Within the infrared branch, frequency-domain feature decomposition and extraction are employed to isolate Gaussian and stripe noise. In the visible-light branch, Retinex decomposition is applied to extract illumination and reflectance components, enabling complementary enhancement of detail and illumination distribution. Subsequently, FILGF performs interactive multi-scale local-global feature fusion. Local feature fusion consists of intra-inter model feature complement, while global feature fusion is achieved through a interactive cross-model attention. Extensive experiments have shown that DAAF outperforms current IVIF algorithms in normal and complex degradation scenarios.

**Index Terms**—Image Fusion, Degradation-Aware Adaptive, Feature Interaction.

## I. INTRODUCTION

Infrared and visible light images exhibit strong complementary characteristics. Specifically, visible images have rich texture details but are susceptible to variations in lighting, while infrared images provide thermal information but lack texture details [1]. Therefore, infrared-visible image fusion (IVIF) can overcome the limitations of noise and low resolution in infrared images, as well as the effects of lighting and camouflage on visible images [2]. This capability is crucial in applications such as autonomous driving [3], person re-identification [4] and night-time target detection [5, 6].

Deep learning-based IVIF methods have evolved into diverse frameworks, including autoencoders (AEs) [12–14], convolutional neural networks (CNNs) [7, 15–17], generative adversarial network (GANs) [18–20], Transformers [8, 21–24], demonstrating significant progress under high-quality image assumptions. However, these approaches largely overlook the prevalent sensor-induced degradations in real-world scenarios. When processing source images with compound degradations (e.g., hybrid noise in infrared images and extreme illumination distortions in visible images), existing methods face dual challenges: Fusion networks based on idealized imaging assumptions struggle to disentangle degradation features from valid information (Fig. 1(b) and Fig. 1(c)); while specialized networks for single degradation types or two-stage preprocessing-

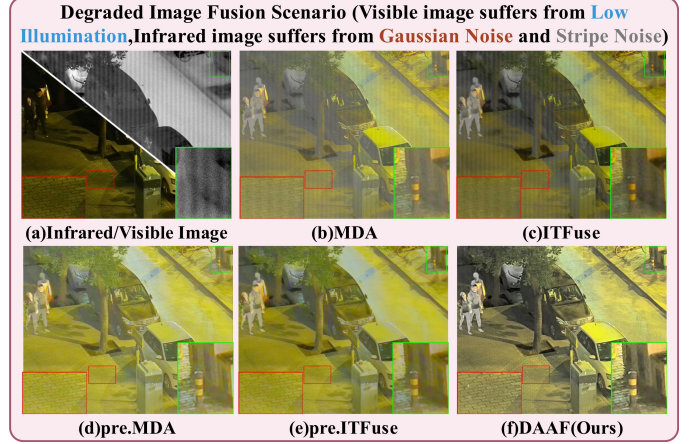


Fig. 1. Image fusion under degradation scenarios: MDA [7] and ITFuse [8] are CNN-based and Transformer-based image fusion method, respectively. "pre." denotes various preprocessing methods (Zero-DCE++ [9]: low-light enhancement, ASCNet [10]: stripe noise removal, Swin-IR [11]: Gaussian noise removal).

fusion pipelines exist, they exhibit inherent drawbacks in multi-modal compound degradation scenarios, including cumbersome degradation perception and decoupled optimization objectives. These limitations result in suboptimal fusion quality for real-world applications (Fig. 1(d) and Fig. 1(e)). The critical challenge lies in achieving synergistic optimization between compound degradation perception and image fusion, which is pivotal for advancing IVIF performance in practical scenarios.

To address the limitations of existing methods in compound degraded image fusion, we emphasize the critical importance of detecting and separating degradation components. As shown in Fig. 2, common illumination degradations in visible images primarily affect the illumination components from Retinex decomposition, while compound noise in infrared images can be separated via frequency-domain decomposition [25]. These decomposition processes simultaneously achieve degradation separation and effective information preservation. Therefore, constructing a degradation-aware adaptive fusion network is pivotal for resolving low-quality fusion in complex degradation scenarios. Key innovations include: (1) simplifying the cumbersome degradation-prior-dependent workflow through unified modeling and adaptive processing within the degradation-aware network, and (2) breaking the error propagation chain in two-stage methods by employing implicit correction to avoid information loss caused by explicit restoration.

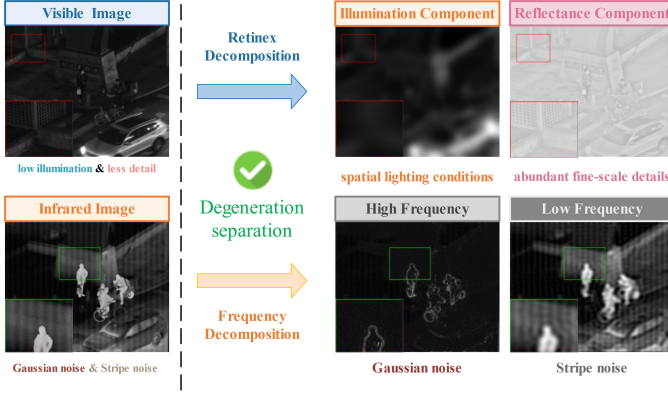


Fig. 2. Decomposed infrared-visible degraded image pairs: visible images are decomposed into illumination (lighting distribution) and reflectance (scene details) components, while infrared images are separated into high-frequency (Gaussian noise) and low-frequency (strip noise) components.

Based on above analysis, we proposed a degradation-aware adaptive fusion (DAAF) framework, including the adaptive degradation optimization network (ADON) and the feature interactive local-global fusion (FILGF) network. The ADON consists of infrared and visible-light branches. The infrared branch utilizes the 2D-Discrete Cosine Transform (2D-DCT) to perform frequency decomposition, effectively separating compound noise. The visible-light branch utilizes Retinex decomposition to extract illumination and reflection components, thereby achieving complementary enhancement of details and illumination distribution. Within FILGF, cross-modal feature interactions are performed on multi-scale local features and global features respectively, achieving efficient complementary feature mining and fusion. The main contribution of our work are as follows:

- 1) We propose DAAF which integrates degradation perception with fusion tasks to mitigate the impact of composite degradations on fusion results.
- 2) We propose the Adaptive Degradation Optimization Network (ADON) that performs adaptive optimization for different modalities and degradation types.
- 3) We propose the Feature Interactive Local-Global Fusion (FILGF) Network that achieves comprehensive feature exploration and fusion through local-global interactions across modalities.

## II. RELATED WORK

### A. Infrared and Visible Image Fusion

The flourishing development of deep learning methods has revitalized new vitality into the IVIF, such as AE [12–14], convolutional neural networks (CNN) [15–17], generative adversarial networks (GAN) [18–20], and vision transformer (ViT) [8, 21–24]. These architectures represent the primary frameworks employed in deep learning-based IVIF methods. Additionally, several approaches have emerged for subsequent advanced visual tasks [26–28], based on semantic driven to limit the fusion network to retain richer semantic information. However, these methods are primarily designed for high-quality images and do not account for the fusion of infrared and visible light

when images exhibit degradation, which can adversely affect the quality of the fused image in practical scenarios.

### B. Degradation-Aware image fusion

To address the issue where degradations in source images degrade fusion quality, specialized fusion networks have been developed [16, 29–31] to address specific degradation interference (e.g., illumination degradation) in source images. Other approaches incorporate textual guidance [32] to achieve targeted optimization for specific degradation types. However, when handling fusion tasks involving compound degradations across modalities (e.g., visible image illumination degradation combined with infrared stripe noise and Gaussian noise), these methods struggle to achieve effective degradation separation and targeted removal.

## III. METHOD

### A. Overall Framework

Network architecture of DAAF is illustrated in Fig. 3, we first convert the visible image to YCbCr color space and extract the Y component with luminance degradation as the degraded visible input. The degraded input images from both modalities  $I_{vi}^{de}, I_{ir}^{de} \in \mathbb{R}^{B \times 1 \times H \times W}$  are then separately processed through ADON to achieve degradation separation and effective feature filtering:

$$f_{vi}^{en} = ADON(I_{vi}^{de}), f_{ir}^{en} = ADON(I_{ir}^{de}) \quad (1)$$

where  $f_{vi}^{en}, f_{ir}^{en} \in \mathbb{R}^{B \times C \times H \times W}$  denote the degradation-removed visible and infrared features output by  $ADON(\cdot)$ . These features are then fed into  $FILGF(\cdot)$  to thoroughly explore multi-scale local deep features representing image details and global deep information characterizing intensity and structural patterns, while establishing effective cross-modal feature interactions for complementary feature fusion:

$$f_{fu} = FILGF(f_{vi}^{en}, f_{ir}^{en}) \quad (2)$$

where  $f_{fu} \in \mathbb{R}^{B \times C \times H \times W}$  denotes the fused features. Finally, a CNN-based image reconstruction module (comprising three cascaded  $3 \times 3$  convolution operations with LeakyReLU activation) maps the fused features to the image space to obtain the network output  $I_{fu}^Y = Re(f_{fu})$ , which serves as the new Y component. This result is then recombined with the visible Cb and Cr components and converted to RGB space to form the final fused image  $I_{fu} \in \mathbb{R}^{B \times 3 \times H \times W}$ .

### B. Interactive Transformer-based Block

Although SwinTransformer [33] exhibits excellent global feature extraction capabilities, it struggles to effectively establish global interactions both among components within a modality and across modalities in the DAAF framework. To address this, we design an Interactive Transformer Block (ITB)

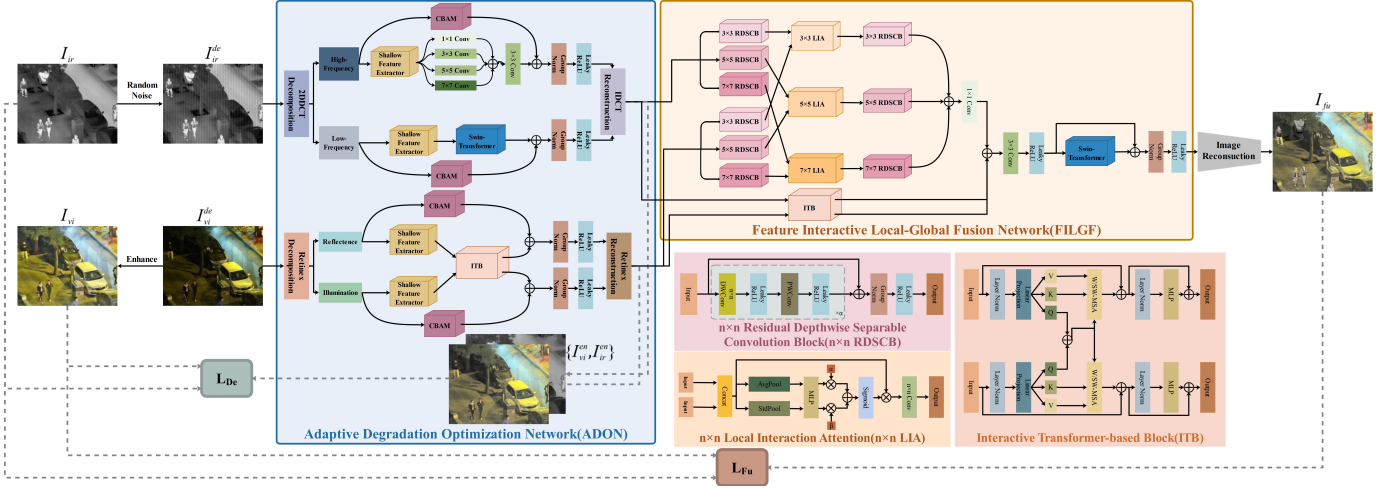


Fig. 3. Overall architecture of the proposed DAAF. The DAAF framework comprises two principal subnetworks: the Adaptive Degradation Optimization Network (ADON) and the Feature Interactive Local-Global Fusion (FILGF) Network. It incorporates three uniquely designed modules: the  $n \times n$  Residual Depthwise Separable Convolution Block ( $n \times n$  RDSCB),  $n \times n$  Local Interaction Attention ( $n \times n$  LIA), and Interactive Transformer-based Block (ITB).

to perform cross-dimensional interaction processing on the input features  $f_1, f_2 \in \mathbb{R}^{B \times C \times H \times W}$ :

$$\begin{aligned} f_1^{ISA} &= ISA(LN(f_1), LN(f_2)) + f_1 \\ f_1^{out} &= FFN(LN(f_1^{ISA})) + f_1^{ISA} \\ f_2^{ISA} &= ISA(LN(f_2), LN(f_1)) + f_2 \\ f_2^{out} &= FFN(LN(f_2^{ISA})) + f_2^{ISA} \end{aligned} \quad (3)$$

The ITB generates dual output features  $f_1^{out}, f_2^{out} \in \mathbb{R}^{B \times C \times H \times W}$ . Unlike multi-head self-attention (MSA), our interactive self-attention ( $ISA(\cdot)$ ) mechanism enables cross-component/modality interaction through shared-query computation. For input windows  $X^1, X^2 \in \mathbb{R}^{M^2 \times C}$ , the ISA mechanism operates as:

$$\begin{aligned} \{Q_1, K_1, V_1\} &= \{X_1 W^{Q1}, X_1 W^{K1}, X_1 W^{V1}\} \\ \{Q_2, K_2, V_2\} &= \{X_2 W^{Q2}, X_2 W^{K2}, X_2 W^{V2}\} \\ X_1^{ISA} &= MSA(Q_1 + Q_2, K_1, V_1) \\ X_2^{ISA} &= MSA(Q_2 + Q_1, K_2, V_2) \end{aligned} \quad (4)$$

where  $X_1^{ISA}, X_2^{ISA} \in \mathbb{R}^{M^2 \times C}$  represent the output window features by ISA. Thus, ITB achieves coordinated optimization of intra-feature global modeling and cross-feature interaction learning.

### C. Adaptive Degradation Optimization Network (ADON)

To simplify the cumbersome degradation-prior-dependent workflows and achieve implicit degradation correction, we propose the Adaptive Degradation Optimization Network (ADON). As shown in Fig. 3, ADON performs Retinex decomposition for visible images and frequency decomposition for infrared images, aiming to achieve degradation separation for subsequent targeted removal and preliminary extraction of fusion-relevant information:

$$\begin{aligned} \{f_{low}, f_{high}\} &= 2DDCT(I_{ir}^{de}) \\ \{f_R, f_L\} &= Retinex(I_{vi}^{de}) \end{aligned} \quad (5)$$

where  $f_{low}, f_{high} \in \mathbb{R}^{B \times C \times H \times W}$  denote the low-high frequency components obtained by  $2DDCT(\cdot)$  to the degraded infrared image  $I_{ir}^{de}$ , while  $f_R, f_L \in \mathbb{R}^{B \times C \times H \times W}$  represent the reflectance and illumination components derived from  $Retinex(\cdot)$  decomposition of the degraded visible image  $I_{vi}^{de}$ .

After shallow feature extraction of the four components, we design dedicated feature extraction methods tailored to the inherent characteristics of different modality-specific components. For  $f_{low}$  and  $f_{high}$ , we employ multi-scale convolution and Swin Transformer ( $SwinTrm(\cdot)$ ) [33] to fully extract high-frequency features (detail information) and low-frequency features (structural information) while filtering noise. Efficient CBAM attention mechanisms ( $CBAM(\cdot)$ ) [34] are inserted into residual connections to achieve further emphasis on key information and degradation filtering:

$$\begin{aligned} f'_{high} &= Conv_3(Concat(ConvBlock_n(SF(f_{high})))) \\ f_{high}^{en} &= LReLU(GN(f'_{high} + CBAM(f_{high}))) \\ f'_{low} &= SwinTrm(SF(f_{low})) \\ f_{low}^{en} &= LReLU(GN(f'_{low} + CBAM(f_{low}))) \end{aligned} \quad (6)$$

where  $f_{high}^{en}, f_{low}^{en} \in \mathbb{R}^{B \times C \times H \times W}$  denote the enhanced high and low-frequency features.  $Conv_3(\cdot)$  denotes a  $3 \times 3$  convolution,  $SF(\cdot)$  consists of three consecutive  $Conv_3(\cdot)$  operations, while  $ConvBlock_n(\cdot)$  combines a convolution operation with kernel size  $n$  (where  $n = \{1, 3, 5, 7\}$ ) and Leaky ReLU activation  $LReLU(\cdot)$  to extract multi-scale high-frequency infrared features.  $Concat(\cdot)$  indicates channel-wise concatenation,  $GN(\cdot)$  represents Group Normalization. Finally, we reconstruct enhanced spatial-domain features through the IDCT Reconstruction Block:  $f_{ir}^{en} = IDCT(f_{low}^{en}, f_{high}^{en})$ .

For the visible image components  $f_R$  and  $f_L$ , we utilize the Interactive Transformer-based Block  $ITB(\cdot)$  to enhance the illumination component and extract valid information from the reflectance component through inter-component interaction, while embedding CBAM attention mechanisms [34] into



residual connections:

$$\begin{aligned} \{f'_R, f'_L\} &= ITB(SF(f_R), SF(f_L)) \\ f_R^{en} &= LReLU(GN(f'_R + CBAM(f_R))) \\ f_L^{en} &= LReLU(GN(f'_L + CBAM(f_L))) \end{aligned} \quad (7)$$

where  $f_R^{en}, f_L^{en} \in \mathbb{R}^{B \times C \times H \times W}$  denote the enhanced reflectance and illumination components respectively. Finally, we reconstruct the spatial-domain enhanced visible features by performing element-wise multiplication of the two components:  $f_{vi}^{en} = f_R^{en} \otimes f_L^{en}$ .

Through ADON, we obtain enhanced features for both modalities  $f_{vi}^{en}, f_{ir}^{en} \in \mathbb{R}^{B \times C \times H \times W}$ . During the ADON training phase, the enhanced features are fed into a CNN-based decoder and mapped to the image space to generate enhanced images for both modalities, which are then used to compute losses with non-degraded source images. In FILGF training, ADON solely outputs enhanced features of both modalities as inputs to FILGF for subsequent feature fusion.

#### D. Feature Interactive Local-Global Fusion (FILGF) Network

1) **Residual Depthwise Separable Convolution Block:** To thoroughly extract multi-scale detail information, we design a Residual Depthwise Separable Convolution Block (RDSCB). It consists of the depthwise convolution block  $DCB_n(\cdot)$  (with  $n \times n$  convolution and LeakyReLU) to aggregate spatial features, followed by the point-wise convolution block  $PCB(\cdot)$  (containing point-wise convolution and LeakyReLU) for channel-wise interaction. This procedure is iterated  $\alpha$  times to achieve deep information mining:

$$\begin{aligned} f' &= (PCB(DCB_n(f_{in})))^\alpha \\ f_{out} &= LReLU(GN(f' + f_{in})) \end{aligned} \quad (8)$$

where  $f_{in}, f_{out} \in \mathbb{R}^{B \times C \times H \times W}$  are the input and output of RDSCB.

2) **Local Interaction Attention:** To enhance cross-modal local interaction and complementary feature fusion, we propose the Local Interaction Attention (LIA) mechanism. For input features  $f_1, f_2 \in \mathbb{R}^{B \times C \times H \times W}$ , LIA first applies spatial average pooling ( $AvgPool(\cdot)$ ) and standard deviation pooling ( $StdPool(\cdot)$ ) to capture modality-specific saliency maps. These are processed through a MLP to learn nonlinear channel-wise correlations, followed by an adaptive weighting mechanism using learnable parameters  $\alpha$  and  $\beta$ . The resulting attention maps, activated via  $Sigmoid(\cdot)$ , are element-wise multiplied with original features and refined through kernel-adaptive convolutions for dimensional alignment:

$$\begin{aligned} f' &= Concat(f_1, f_2) \\ Att_{f'} &= \alpha MLP(Avgpool(f')) + \beta MLP(Stdpool(f')) \\ f_{out} &= Conv_n(Sigmoid(Att_{f'}) \times f') \end{aligned} \quad (9)$$

where  $f_{out} \in \mathbb{R}^{B \times C \times H \times W}$  denotes the locally fused features.

3) **Architecture:** The structure of FILGF is shown in Fig. 3. We implement feature fusion through separate multi-scale local feature and global feature branches. The multi-scale local feature branch takes the ADON-enhanced features  $f_{vi}^{en}, f_{ir}^{en}$  as input, and employs multi-kernel RDSCBs (with kernel sizes 3/5/7) to extract intra-modal multi-scale local features.

Subsequently, features from the same scale but different modalities are fed into cascaded LIA modules and RDSCBs to focus on key information, facilitate feature interaction, and enable deeper local feature mining:

$$\begin{aligned} f_{vi}^n &= RDSCB_{vi}^n(f_{vi}^{en}), f_{ir}^n = RDSCB_{ir}^n(f_{ir}^{en}) \\ f_{fu}^n &= RDSCB^n(LIA(f_{vi}^n, f_{ir}^n)) \\ f^L &= Conv_1(Concat(f_{fu}^n)), n \in \{3, 5, 7\} \end{aligned} \quad (10)$$

where  $f_{vi}^n, f_{ir}^n \in \mathbb{R}^{B \times C \times H \times W}$  denote the intra-model multi-scale features of visible and infrared modalities at scale  $n$ , respectively.  $f_{fu}^n, f^L \in \mathbb{R}^{B \times C \times H \times W}$  represent the scale- $n$  fused features and final local fusion features.  $RDSCB_{vi}^n(\cdot)$ ,  $RDSCB_{ir}^n(\cdot)$ , and  $RDSCB^n(\cdot)$  correspond to the intra-model visible RDSCB module, infrared RDSCB module, and inter-model RDSCB module with kernel size  $n$ .

For the global feature fusion branch, we employ the  $ITB(\cdot)$  to achieve global feature complementary enhancement:

$$\{f_{vi}^G, f_{ir}^G\} = ITB(f_{vi}^{en}, f_{ir}^{en}) \quad (11)$$

where  $f_{vi}^G, f_{ir}^G \in \mathbb{R}^{B \times C \times H \times W}$  represent the globally enhanced visible and infrared features obtained through deep global feature extraction and cross-modal complementary enhancement.

After establishing inter-modal relationships between local-local and global-global features, we further explore correlations between local-global features through subsequent convolutions and Swin Transformer  $SwinTrm(\cdot)$  [33]:

$$\begin{aligned} f'_{fu} &= LReLU(Conv_3(Concat(f_{vi}^G, f_{ir}^G, f^L))) \\ f_{fu} &= LReLU(GN(SwinTrm(f'_{fu}) + f'_{fu})) \end{aligned} \quad (12)$$

where  $f_{fu} \in \mathbb{R}^{B \times C \times H \times W}$  denote the final fused features.

#### E. Loss Function

1) **Degradation Optimization Loss:** To ensure that our ADON can effectively separate degradations and retain useful information, we design a degradation optimization loss function composed of three sub-functions:

$$\mathcal{L}_{De} = \mathcal{L}_{ir} + \mathcal{L}_{vi} + \mathcal{L}_{Re} \quad (13)$$

where  $\mathcal{L}_{ir}$  and  $\mathcal{L}_{vi}$  denote the reconstruction loss functions for infrared and visible images, respectively. These loss functions impose pixel-level constraints on the enhanced images to maximally preserve valid information. Both loss functions are constructed based on the Charbonnier loss formulation [35], expressed as:

$$\begin{aligned} \mathcal{L}_{ir} &= \frac{1}{HW} \sqrt{(I_{ir} - \tilde{I}_{ir})^2 + \varepsilon} \\ \mathcal{L}_{vi} &= \frac{1}{HW} \sqrt{(I_{vi} - \tilde{I}_{vi})^2 + \varepsilon} \end{aligned} \quad (14)$$

where  $I_{ir}$  and  $I_{vi}$  represent the non-degraded infrared and visible images,  $\tilde{I}_{ir}$  and  $\tilde{I}_{vi}$  denote the reconstructed infrared and visible images from ADON,  $\varepsilon$  is a constant set to 1e-6 during training, and  $H, W$  indicate the image height and width. Additionally, we employ  $\mathcal{L}_{Re}$  to achieve more comprehensive degradation removal, which comprises three



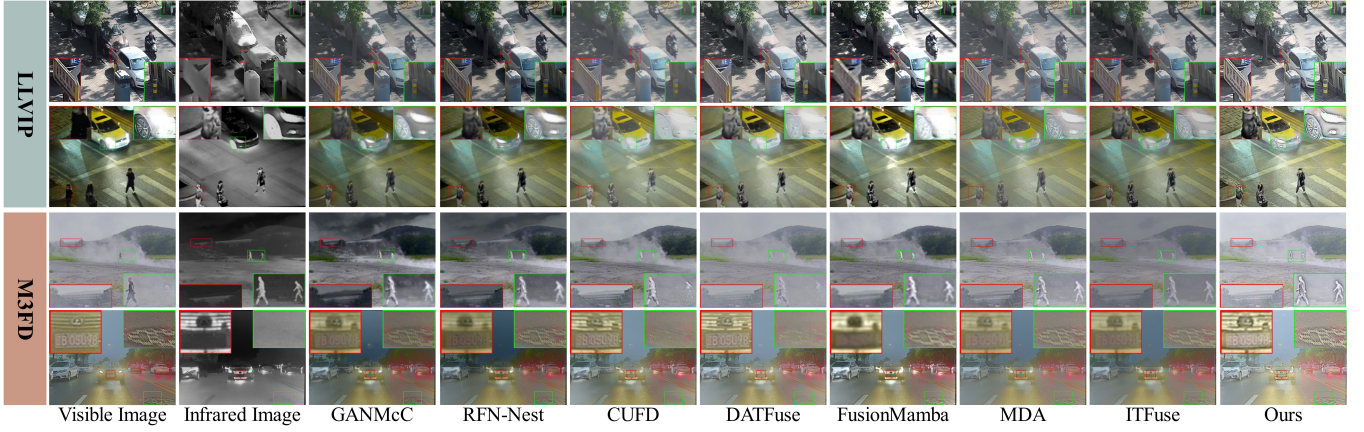


Fig. 4. Qualitative comparison of DAAF and seven comparative methods on the LLVIP (top two rows) and M3FD (bottom two rows) datasets, key regions are marked with red and green boxes and enlarged to simplify visual comparison.

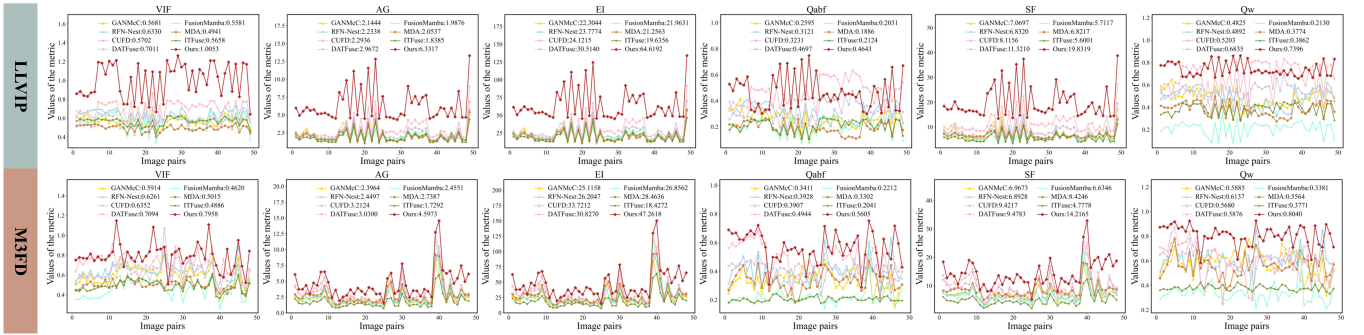


Fig. 5. Quantitative comparison of individual metrics for DAAF and seven comparative methods on the LLVIP (first row) and M3FD (second row) datasets. The red line represents our method, with the average value for each metric displayed above the line. Higher value indicates better performance.

components: illumination loss  $\mathcal{L}_{illu}$ , total variation loss  $\mathcal{L}_{TV}$ , and infrared perception loss  $\mathcal{L}_{per}$ :

$$\mathcal{L}_{Re} = \alpha_1 \mathcal{L}_{illu} + \alpha_2 \mathcal{L}_{TV} + \alpha_3 \mathcal{L}_{per} \quad (15)$$

where  $\alpha_1$ ,  $\alpha_2$ , and  $\alpha_3$  are weighting coefficients for balancing the three loss functions. The illumination loss  $\mathcal{L}_{illu}$  enforces more reasonable and smoother brightness distribution in enhanced visible images by computing average intensity differences across image patches, which can be expressed as:

$$\begin{aligned} L_{vi} &= Avgpool_{16 \times 16}(I_{vi}), \tilde{L}_{vi} = Avgpool_{16 \times 16}(\tilde{I}_{vi}) \\ \mathcal{L}_{illu} &= \frac{16 \times 16}{HW} \sqrt{(L_{vi} - \tilde{L}_{vi})^2 + \varepsilon} \end{aligned} \quad (16)$$

where  $I_{vi}$  and  $\tilde{I}_{vi}$  denote the non-illumination-degraded visible image and the ADON-reconstructed visible image, respectively.  $L_{vi}$  and  $\tilde{L}_{vi}$  represent their corresponding illumination distribution maps, with  $AvgPool_{16 \times 16}(\cdot)$  indicating the  $16 \times 16$  patch-based average pooling operation. The total variation loss  $\mathcal{L}_{TV}$  promotes image smoothing and noise reduction by minimizing the total variation:

$$\begin{aligned} \mathcal{L}_{TV}(x) &= \frac{1}{(H-1)W} \sum_{i=1}^{H-1} \sum_{j=1}^W (x_{i+1,j} - x_{i,j})^2 \\ &+ \frac{1}{H(W-1)} \sum_{i=1}^H \sum_{j=1}^{W-1} (x_{i,j+1} - x_{i,j})^2 \end{aligned} \quad (17)$$

where  $x_{i,j}$  denotes the pixel value at position  $(i,j)$  of the ADON-reconstructed infrared enhanced image  $\tilde{I}_{ir}$ . To prevent effective information loss caused by image denoising and better preserve valuable features from the infrared image, we employ the perceptual loss  $\mathcal{L}_{per}$  to compute feature-level discrepancies, generating enhanced images with rich characteristics.

$$\mathcal{L}_{per} = ||VGG(I_{ir}) - VGG(\tilde{I}_{ir})||_2^2 \quad (18)$$

where  $VGG(\cdot)$  denotes the pre-trained VGG-16 model.

2) **Fusion Loss:** To ensure the fused image generated by the network preserves adequate intensity information and detailed features from the source images, following loss components:

$$\mathcal{L}_{Fu} = \beta_1 \mathcal{L}_{int} + \beta_2 \mathcal{L}_{grad} \quad (19)$$

where  $\beta_1$  and  $\beta_2$  are weighting coefficients to balance the two sub-loss functions. We employ the intensity loss function  $\mathcal{L}_{int}$  to ensure sufficient intensity information preservation in the fused image:

$$\mathcal{L}_{int} = \frac{1}{HW} (||I_{fu} - I_{ir}||_1 + ||I_{fu} - I_{vi}||_1) \quad (20)$$

where  $I_{fu}$ ,  $I_{ir}$ , and  $I_{vi}$  represent the fused image, infrared image, and visible image, respectively. Additionally, we introduce the texture loss  $\mathcal{L}_{text}$  to maximally preserve detail information derived from the source images:

$$\mathcal{L}_{text} = \frac{1}{HW} |||\nabla I_{fu}| - \max(|\nabla I_{ir}|, |\nabla I_{vi}|)||_1 \quad (21)$$

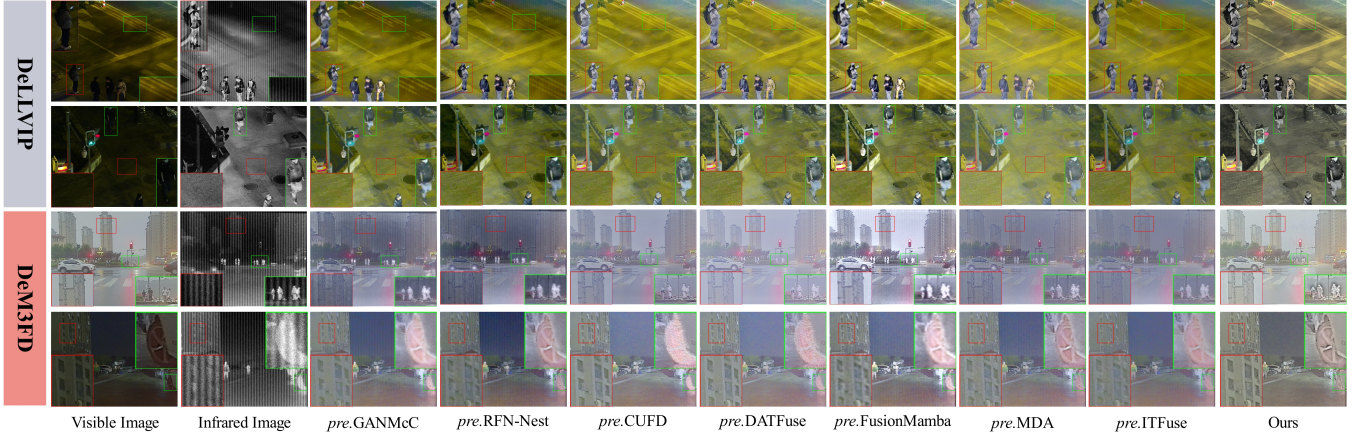


Fig. 6. Qualitative comparison of DAAF and seven comparative methods on the DeLLVIP (top two rows) and DeM3FD (bottom two rows) datasets, key regions are marked with red and green boxes and enlarged to simplify visual comparison. "pre." denotes various preprocessing methods (Zero-DCE++ [9]: low-light enhancement, ASCNet [10]: stripe noise removal, Swin-IR [11]: Gaussian noise removal)

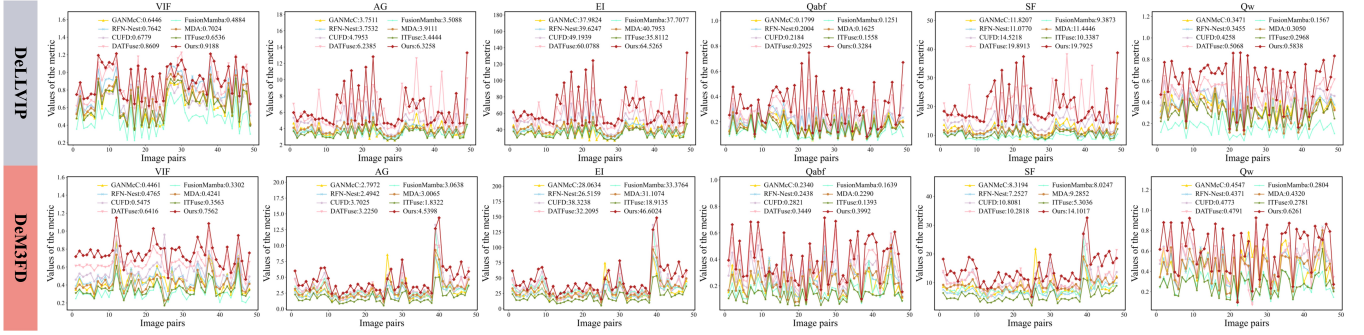


Fig. 7. Quantitative comparison of individual metrics for DAAF and seven comparative methods on the DeLLVIP (first row) and DeM3FD (second row) datasets. The red line represents our method, with the average value for each metric displayed above the line. Higher value indicates better performance.

where  $\nabla$  is Sobel gradient operator,  $\max(\cdot)$  denotes the element-wise maximum selection.

#### IV. EXPERIMENTS

##### A. Experimental Settings

**Implementation details:** For DAAF training, we randomly selected 4,725 image pairs from the LLVIP[36] training set. First, random intensities of Gaussian noise, stripe noise, or a combination of both were added to the original infrared images. These noisy infrared images and the original brightness-degraded visible light images were then used as network inputs. The loss function was then computed between the ADON output and the enhanced visible images obtained via Zero-DCE++ [9] along with the original noise-free infrared images. Specifically, during FILGF training, we load the pre-trained ADON model with frozen parameters, utilizing only ADON's output features as FILGF inputs to train both FILGF and the Image Reconstruction Block.

For ADON training, We randomly cropped pairs of image patches with dimensions  $128 \times 128$  from the LLVIP [36], normalizing pixel intensity to the range  $[0, 1]$ . The Adam optimizer was employed with a learning rate of  $1 \times 10^{-3}$  and a batch size of 16. It is worth noting that during the training of FILGF, the parameter settings are exactly the same

as those of ADON. The hyperparameters of the loss function,  $\alpha_1$ ,  $\alpha_2$ ,  $\alpha_3$ ,  $\beta_1$  and  $\beta_2$  were empirically set to 1, 100, 1, 1 and 5, respectively. All experiments were conducted on a NVIDIA GeForce RTX 4090D GPU. Finally, we evaluate DAAF on the LLVIP [36] and M3FD [28] datasets to assess the performance.

**Comparative methods and evaluation metrics:** We selected AE-based methods RFN-Nest [12] and CUFD [37], CNN-based methods MDA[7], GAN-based method GANMcC [19], Transformer-based method DATFuse [22] and ITFuse[8], Mamba-based method FusionMamba [38]. Additionally, we employed six widely recognized metrics for quantitative evaluation, including visual information fidelity (VIF) [39], average gradient (AG) [40], edge Intensity (EI) [41], gradient-based similarity measurement ( $Q_{abf}$ ) [42], spatial frequency (SF) [43], peilla's metric( $Q_w$ ) [44].

##### B. Image Fusion in Practical Scenarios

1) *Qualitative Analysis:* Fig. 4 presents qualitative analysis of fusion results on LLVIP and M3FD datasets, highlighting critical regions for visual comparison. GANMcC and RFN-Nest tend to inherit background intensity from infrared images, resulting in low contrast (red and green boxes in Row 3 and 4). CUFD and DATFuse exhibit limitations in preserving visible details and retaining critical infrared targets, leading to information loss (red box in Row 1 and green box in Row 3).



TABLE I

QUANTITATIVE COMPARISON BETWEEN DAAF AND SEVEN FUSION METHODS ON PRACTICAL (LLVIP, M3FD) AND CHALLENGE (DeLLVIP, DeM3FD) SCENARIOS, WITH THE TOP THREE METHODS FOR EACH METRIC HIGHLIGHTED IN RED, BLUE, AND GREEN RESPECTIVELY.  $\uparrow$  INDICATES THAT HIGHER VALUES CORRESPOND TO BETTER PERFORMANCE.

Method	Practical Scenarios(LLVIP/M3FD)						Challenge Scenarios(DeLLVIP/DeM3FD)					
	VIF $\uparrow$	AG $\uparrow$	EF $\uparrow$	$Q_{abf} \uparrow$	SF $\uparrow$	$Q_w \uparrow$	VIF $\uparrow$	AG $\uparrow$	EF $\uparrow$	$Q_{abf} \uparrow$	SF $\uparrow$	$Q_w \uparrow$
GANMcC[19]	0.5681 / 0.5914	2.1444 / 2.3964	22.3044 / 25.1158	0.2595 / 0.3411	7.0697 / 6.9673	0.4825 / 0.5885	0.6446 / 0.4461	3.7511 / 2.7972	37.9824 / 28.0634	0.1799 / 0.2340	11.8207 / 8.3194	0.3471 / 0.4547
RFN-Nest[12]	<b>0.6330</b> / 0.6261	2.2338 / 2.4497	23.7774 / 26.2047	0.3121 / 0.3928	6.8320 / 6.8928	0.4892 / <b>0.6137</b>	<b>0.7642</b> / 0.4765	3.7532 / 2.4942	39.6247 / 26.5159	0.2004 / 0.2438	11.0770 / 7.2527	0.3455 / 0.4371
CUFD[37]	<b>0.5702</b> / <b>0.6352</b>	<b>2.2936</b> / <b>3.2124</b>	<b>24.1215</b> / <b>33.7212</b>	<b>0.3231</b> / 0.3907	<b>8.1156</b> / <b>9.4217</b>	<b>0.5203</b> / 0.5680	<b>0.6779</b> / <b>0.5475</b>	<b>4.7953</b> / <b>3.7025</b>	<b>49.1939</b> / <b>38.3238</b>	<b>0.2184</b> / <b>0.2821</b>	<b>14.5218</b> / <b>10.8081</b>	<b>0.4258</b> / 0.4773
DATFuse[22]	<b>0.7011</b> / <b>0.7094</b>	<b>2.9672</b> / <b>3.0300</b>	<b>30.5140</b> / <b>30.8270</b>	<b>0.4697</b> / 0.4944	<b>11.3210</b> / <b>9.4783</b>	<b>0.6835</b> / 0.5876	<b>0.8609</b> / <b>0.6416</b>	<b>6.2385</b> / <b>3.2250</b>	<b>60.0788</b> / <b>32.2095</b>	<b>0.2925</b> / <b>0.3449</b>	<b>19.8913</b> / <b>10.2818</b>	<b>0.5068</b> / 0.4791
FusionMamba[38]	0.5581 / 0.4620	1.9876 / 2.4551	21.9631 / 26.8562	0.2031 / 0.2212	5.7117 / 6.6346	0.2130 / 0.3381	0.4884 / 0.3302	3.5088 / 3.0638	37.7077 / 33.3764	0.1251 / 0.1639	9.3873 / 8.0247	0.1567 / 0.2804
MDA[7]	0.4941 / 0.5015	2.0537 / 2.7387	21.2563 / 28.4636	0.1886 / 0.3302	6.8217 / 8.4246	0.3774 / 0.5564	0.7024 / 0.4241	3.9111 / 3.0065	40.7953 / 31.1074	0.1625 / 0.2290	11.4446 / 9.2852	0.3050 / 0.4320
ITFuse[8]	0.5658 / 0.4886	1.8385 / 1.7292	19.6356 / 18.4272	0.2124 / 0.2041	5.6001 / 4.7778	0.3862 / 0.3771	0.6536 / 0.3563	3.4444 / 1.8322	35.8112 / 18.9135	0.1558 / 0.1393	10.3387 / 5.3036	0.2968 / 0.2781
<b>*Ours</b>	<b>1.0053</b> / <b>0.7958</b>	<b>6.3317</b> / <b>4.5973</b>	<b>64.6193</b> / <b>47.2618</b>	<b>0.4643</b> / <b>0.5605</b>	<b>19.8319</b> / <b>14.2165</b>	<b>0.7396</b> / <b>0.8040</b>	<b>0.9188</b> / <b>0.7562</b>	<b>6.3258</b> / <b>4.5398</b>	<b>64.5265</b> / <b>46.6024</b>	<b>0.3284</b> / <b>0.3992</b>	<b>19.7925</b> / <b>14.1017</b>	<b>0.5838</b> / <b>0.6261</b>

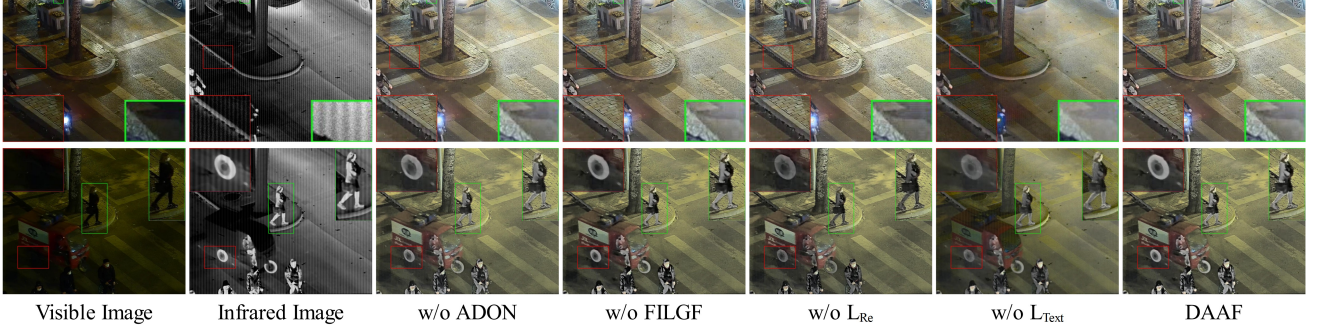


Fig. 8. Qualitative comparison of DAAF ablation experiments, the key regions in the images are marked with red and green boxes and enlarged for ease of observation and comparison.

FusionMamba struggles to extract sufficient details from both sources, causing missing or blurred details (green boxes in Row 1-2). CUFD and DATFuse show limited infrared information extraction (green box in Row 3). CUFD, DATFuse, and FusionMamba struggle to preserve salient details and edges from source images in noisy environments (red box in Row 2; green/red boxes in Row 4). MDA and ITFuse fail to maintain proper contrast in fused results (red box in Row 3). Furthermore, two-stage approaches cannot eliminate residual noise from preprocessing during fusion (stripe noise in Row 1 green box; Gaussian noise in Row 2 red box; mixed noise in Rows 3-4), with all seven compared methods exhibiting varying degrees of color distortion. DAAF effectively eliminates degradations and fuses valuable information through single-stage degradation separation and cross-modal complementarity, producing visually natural and perceptually superior images.

2) *Quantitative Analysis*: Quantitative analysis of DAAF against seven comparative methods on LLVIP and M3FD datasets is presented in Fig. 5 and Tab. I. Although our method shows marginally lower performance than DATFuse in the  $Q_{abf}$  metric on the LLVIP dataset, it achieves substantial improvements across all five remaining metrics on LLVIP and all evaluation metrics on M3FD. These results demonstrate DAAF's superior capability to extract effective information from source images and generate fused images with enhanced visual quality and rich detail preservation.

### C. Image Fusion in Challenge Scenarios

To validate DAAF's superiority in fusing degraded images (infrared with Gaussian/strip noise, visible with illumination degradation), we constructed DeLLVIP and DeM3FD datasets using randomly selected test pairs from LLVIP (50 pairs) and M3FD (49 pairs). Visible images retained original illumination degradation while infrared images were augmented with random-intensity Gaussian/strip noise mixtures. In two-stage comparisons, visible images were enhanced with Zero-DCE++ [9] and infrared images were preprocessed using ASCNet [10] (destriping) and Swin-IR [11] (denoising), followed by fusion with seven state-of-the-art methods.

1) *Qualitative Analysis*: Fig. 6 demonstrates image fusion comparisons under complex degradation conditions. GAN-McC and RFN-Nest exhibit imbalanced intensity inheritance from source images, failing to achieve satisfactory visible

illumination and causing contrast reduction (green boxes in Rows 1 & 3). CUFD and DATFuse show limited infrared information extraction (green box in Row 3). CUFD, DATFuse, and FusionMamba struggle to preserve salient details and edges from source images in noisy environments (red box in Row 2; green/red boxes in Row 4). MDA and ITFuse fail to maintain proper contrast in fused results (red box in Row 3). Furthermore, two-stage approaches cannot eliminate residual noise from preprocessing during fusion (stripe noise in Row 1 green box; Gaussian noise in Row 2 red box; mixed noise in Rows 3-4), with all seven compared methods exhibiting varying degrees of color distortion. DAAF effectively eliminates degradations and fuses valuable information through single-stage degradation separation and cross-modal complementarity, producing visually natural and perceptually superior images.

2) *Quantitative Analysis*: Fig. 7 and Tab. I demonstrates that DAAF achieves superior performance on five evaluation metrics in DeLLVIP and all metrics in DeM3FD except marginally lower SF than DATFuse in DeLLVIP. These results confirm that compared to two-stage fusion methods, our DAAF more effectively implements degradation removal and critical information preservation for degraded image fusion, while leveraging inter-modal complementary features to generate fused images with clean backgrounds, clear details and rich complementary information.

### D. Ablation Study

1) *Qualitative Analysis*: To validate the effectiveness of DAAF, we conducted ablation studies from the structure and loss function, with the qualitative analysis shown in Fig. 8. 1) When ADON is removed, the network exhibits clear shortcomings in handling degradation in the source images, the fused results show insufficient contrast (green box in the first



TABLE II

QUANTITATIVE COMPARISON OF ABLATION EXPERIMENTS. **RED** REPRESENTS THE BEST RESULT. **REVERSE** REPRESENTS APPLYING SSM TO LOW-FREQUENCY PART.  $\uparrow$  INDICATES THAT HIGHER METRICS THE BETTER PERFORMANCE.

	VIF $\uparrow$	AG $\uparrow$	EI $\uparrow$	$Q_{abf}\uparrow$	SF $\uparrow$	$Q_w\uparrow$
w/o ADON	1.0057	6.0064	61.5511	0.3246	18.8462	0.5671
w/o FILGF	0.8643	5.7803	59.2956	0.3169	17.6852	0.5750
w/o $L_{Re}$	<b>1.0205</b>	6.1119	62.3288	0.3076	19.3660	0.5482
w/o $L_{text}$	0.5402	2.8786	30.2643	0.2159	7.8931	0.3599
<b>*DAAF</b>	0.9188	<b>6.3258</b>	<b>64.5265</b>	<b>0.3284</b>	<b>19.7924</b>	<b>0.5838</b>

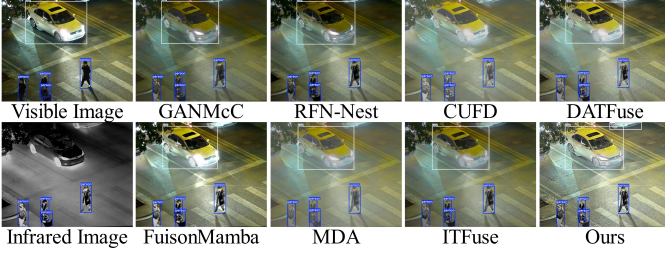


Fig. 9. Detection performance of DAAF and seven comparison methods on fused image from LLVIP dataset.

row) and inherit noise degradation from the infrared images (red boxes in the first and second rows). 2) When FILGF is removed, the fused results fail to adequately extract and fuse edge details, as evidenced by the tire in the red box of the second row and the shadow in the green box of the first row. 3) When  $L_{Re}$  is removed, ADON does not sufficiently optimize the degraded image (striped noise in the red box of the first row) and struggles to effectively preserve the details and intensity information from the source images (red and green boxes in the second row). 4) When  $L_{text}$  is removed, the fused images exhibit a significant loss of edge and detail information, making it difficult to generate fusion images with good visual quality.

2) *Quantitative Analysis*: Quantitative analysis of the ablation studies is shown in Tab. II. After removing ADON or  $L_{Re}$ , although VIF increases indicating that more visual features from the source images are inherited—the corresponding fusion results exhibit significant noise degradation, and the decline in the other five metrics to varying degrees reflects insufficient optimization of source image degradation. When FILGF is removed, AG, EI, and SF drop significantly, demonstrating that FILGF is effective in extracting edge information at different scales from the source images. When  $L_{text}$  is removed, all metrics experience a substantial decline, indicating that  $L_{text}$  is crucial in the image fusion task.

#### E. Extension Experiment

To demonstrate the superiority of DAAF in downstream object detection tasks, we applied the YOLOv5 to fusion results with the comparative methods. In Fig. 9, we conducted a qualitative comparison of the detection results on the fused images. The results show that, compared to other fusion methods where missed detections (such as the vehicle in

the upper right) and incomplete bounding boxes (such as the pedestrian in the lower left) are common, our method is capable of comprehensively detecting targets in the image. This also proves that our method not only compensates for the subpar detection performance of single-modality images due to inherent limitations, but also outperforms other fusion algorithms in downstream tasks.

#### V. CONCLUSION

This paper proposes a Degradation-Aware Adaptive Fusion (DAAF) framework, which achieves unified modeling of adaptive degradation optimization and image fusion, addressing the limitations of existing IVIF methods in handling complex degraded image fusion tasks. The framework includes: the Adaptive Degradation Optimization Network (ADON) that performs adaptive degradation separation and removal through modality-specific decomposition processes while preserving valid information; the Feature Interactive Local-Global Fusion (FILGF) Network that achieves comprehensive fusion of multi-scale local features and global contextual features. Extensive experimental results demonstrate that our DAAF exhibits superior degradation suppression and fusion performance compared to existing IVIF methods.

#### REFERENCES

- [1] J. Ma, Y. Ma, and C. Li, “Infrared and visible image fusion methods and applications: A survey,” *Information fusion*, vol. 45, pp. 153–178, 2019. **1**
- [2] S. Karim, G. Tong, J. Li, A. Qadir, U. Farooq, and Y. Yu, “Current advances and future perspectives of image fusion: A comprehensive review,” *Information Fusion*, vol. 90, pp. 185–217, 2023. **1**
- [3] S. Abrecht, A. Hirsch, S. Raafatnia, and M. Woehrle, “Deep learning safety concerns in automated driving perception,” *IEEE Transactions on Intelligent Vehicles*, 2024. **1**
- [4] X. Cai, L. Liu, L. Zhu, and H. Zhang, “Dual-modality hard mining triplet-center loss for visible infrared person re-identification,” *Knowledge-Based Systems*, vol. 215, p. 106772, 2021. **1**
- [5] C. Hu, Y. Huang, K. Li, L. Zhang, C. Long, Y. Zhu, T. Pu, and Z. Peng, “Datransnet: dynamic attention transformer network for infrared small target detection,” *IEEE Geoscience and Remote Sensing Letters*, 2025. **1**
- [6] M. Xiao, Q. Dai, Y. Zhu, K. Guo, H. Wang, X. Shu, J. Yang, and Y. Dai, “Background semantics matter: Cross-task feature exchange network for clustered infrared small target detection with sky-annotated dataset,” *arXiv preprint arXiv:2407.20078*, 2024. **1**
- [7] G. Yang, J. Li, H. Lei, and X. Gao, “A multi-scale information integration framework for infrared and visible image fusion,” *Neurocomputing*, vol. 600, p. 128116, 2024. **1, 6, 7**
- [8] W. Tang, F. He, and Y. Liu, “Itfuse: An interactive transformer for infrared and visible image fusion,” *Pattern Recognition*, vol. 156, p. 110822, 2024. **1, 2, 6, 7**

- [9] C. Li, C. Guo, and C. C. Loy, "Learning to enhance low-light image via zero-reference deep curve estimation," *IEEE transactions on pattern analysis and machine intelligence*, vol. 44, no. 8, pp. 4225–4238, 2021. 1, 6, 7
- [10] S. Yuan, H. Qin, X. Yan, S. Yang, S. Yang, N. Akhtar, and H. Zhou, "Ascnet: Asymmetric sampling correction network for infrared image destriping," *IEEE Transactions on Geoscience and Remote Sensing*, 2025. 1, 6, 7
- [11] J. Liang, J. Cao, G. Sun, K. Zhang, L. Van Gool, and R. Timofte, "Swinir: Image restoration using swin transformer," in *Proceedings of the IEEE/CVF international conference on computer vision*, 2021, pp. 1833–1844. 1, 6, 7
- [12] H. Li, X.-J. Wu, and J. Kittler, "Rfn-nest: An end-to-end residual fusion network for infrared and visible images," *Information Fusion*, vol. 73, pp. 72–86, 2021. 1, 2, 6, 7
- [13] H. Li and X.-J. Wu, "Densefuse: A fusion approach to infrared and visible images," *IEEE Transactions on Image Processing*, vol. 28, no. 5, pp. 2614–2623, 2018.
- [14] J. Liu, X. Fan, J. Jiang, R. Liu, and Z. Luo, "Learning a deep multi-scale feature ensemble and an edge-attention guidance for image fusion," *IEEE Transactions on Circuits and Systems for Video Technology*, vol. 32, no. 1, pp. 105–119, 2021. 1, 2
- [15] H. Xu, J. Ma, J. Jiang, X. Guo, and H. Ling, "U2fusion: A unified unsupervised image fusion network," *IEEE Transactions on Pattern Analysis and Machine Intelligence*, vol. 44, no. 1, pp. 502–518, 2020. 1, 2
- [16] L. Tang, X. Xiang, H. Zhang, M. Gong, and J. Ma, "Divfusion: Darkness-free infrared and visible image fusion," *Information Fusion*, vol. 91, pp. 477–493, 2023. 2
- [17] L. Tang, J. Yuan, H. Zhang, X. Jiang, and J. Ma, "Piafusion: A progressive infrared and visible image fusion network based on illumination aware," *Information Fusion*, vol. 83, pp. 79–92, 2022. 1, 2
- [18] J. Ma, W. Yu, P. Liang, C. Li, and J. Jiang, "Fusiongan: A generative adversarial network for infrared and visible image fusion," *Information fusion*, vol. 48, pp. 11–26, 2019. 1, 2
- [19] J. Ma, H. Zhang, Z. Shao, P. Liang, and H. Xu, "Ganmcc: A generative adversarial network with multiclassification constraints for infrared and visible image fusion," *IEEE Transactions on Instrumentation and Measurement*, vol. 70, pp. 1–14, 2020. 6, 7
- [20] J. Ma, H. Xu, J. Jiang, X. Mei, and X.-P. Zhang, "Ddcgan: A dual-discriminator conditional generative adversarial network for multi-resolution image fusion," *IEEE Transactions on Image Processing*, vol. 29, pp. 4980–4995, 2020. 1, 2
- [21] A. Dosovitskiy, L. Beyer, A. Kolesnikov, D. Weissenborn, X. Zhai, T. Unterthiner, M. Dehghani, M. Minderer, G. Heigold, S. Gelly *et al.*, "An image is worth 16x16 words: Transformers for image recognition at scale," *arXiv preprint arXiv:2010.11929*, 2020. 1, 2
- [22] W. Tang, F. He, Y. Liu, Y. Duan, and T. Si, "Datfuse: Infrared and visible image fusion via dual attention transformer," *IEEE Transactions on Circuits and Systems for Video Technology*, vol. 33, no. 7, pp. 3159–3172, 2023. 6, 7
- [23] Y. Zhu, Y. Ma, F. Fan, J. Huang, K. Wu, and G. Wang, "Towards accurate infrared small target detection via edge-aware gated transformer," *IEEE Journal of Selected Topics in Applied Earth Observations and Remote Sensing*, 2024.
- [24] J. Ma, L. Tang, F. Fan, J. Huang, X. Mei, and Y. Ma, "Swinfusion: Cross-domain long-range learning for general image fusion via swin transformer," *IEEE/CAA Journal of Automatica Sinica*, vol. 9, no. 7, pp. 1200–1217, 2022. 1, 2
- [25] T. Zhang, Y. Zhu, J. Zhao, G. Cui, and Y. Zheng, "Exploring state space model in wavelet domain: An infrared and visible image fusion network via wavelet transform and state space model," *arXiv preprint arXiv:2503.18378*, 2025. 1
- [26] G. Lv, C. Sima, Y. Gao, A. Dong, G. Ma, and J. Cheng, "Sigfusion: Semantic information guided infrared and visible image fusion," *IEEE Transactions on Instrumentation and Measurement*, 2024. 2
- [27] H. Xu, J. Yuan, and J. Ma, "Murf: Mutually reinforcing multi-modal image registration and fusion," *IEEE transactions on pattern analysis and machine intelligence*, vol. 45, no. 10, pp. 12 148–12 166, 2023.
- [28] J. Liu, X. Fan, Z. Huang, G. Wu, R. Liu, W. Zhong, and Z. Luo, "Target-aware dual adversarial learning and a multi-scenario multi-modality benchmark to fuse infrared and visible for object detection," in *Proceedings of the IEEE/CVF conference on computer vision and pattern recognition*, 2022, pp. 5802–5811. 2, 6
- [29] D. Zou and B. Yang, "Infrared and low-light visible image fusion based on hybrid multiscale decomposition and adaptive light adjustment," *Optics and Lasers in Engineering*, vol. 160, p. 107268, 2023. 2
- [30] J. Chen, L. Yang, W. Liu, X. Tian, and J. Ma, "Lenfusion: a joint low-light enhancement and fusion network for nighttime infrared and visible image fusion," *IEEE Transactions on Instrumentation and Measurement*, 2024.
- [31] Q. Yang, Y. Zhang, Z. Zhao, J. Zhang, and S. Zhang, "Iaifnet: an illumination-aware infrared and visible image fusion network," *IEEE Signal Processing Letters*, 2024. 2
- [32] X. Yi, H. Xu, H. Zhang, L. Tang, and J. Ma, "Text-if: Leveraging semantic text guidance for degradation-aware and interactive image fusion," in *Proceedings of the IEEE/CVF Conference on Computer Vision and Pattern Recognition*, 2024, pp. 27 026–27 035. 2
- [33] Z. Liu, Y. Lin, Y. Cao, H. Hu, Y. Wei, Z. Zhang, S. Lin, and B. Guo, "Swin transformer: Hierarchical vision transformer using shifted windows," in *Proceedings of the IEEE/CVF international conference on computer vision*, 2021, pp. 10 012–10 022. 2, 3, 4
- [34] S. Woo, J. Park, J.-Y. Lee, and I. S. Kweon, "Cbam: Convolutional block attention module," in *Proceedings of the European conference on computer vision (ECCV)*, 2018, pp. 3–19. 3
- [35] P. Charbonnier, L. Blanc-Feraud, G. Aubert, and M. Bar-

- laud, "Two deterministic half-quadratic regularization algorithms for computed imaging," in *Proceedings of 1st international conference on image processing*, vol. 2. IEEE, 1994, pp. 168–172. 4
- [36] X. Jia, C. Zhu, M. Li, W. Tang, and W. Zhou, "Llvip: A visible-infrared paired dataset for low-light vision," in *Proceedings of the IEEE/CVF international conference on computer vision*, 2021, pp. 3496–3504. 6
- [37] H. Xu, M. Gong, X. Tian, J. Huang, and J. Ma, "Cufd: An encoder–decoder network for visible and infrared image fusion based on common and unique feature decomposition," *Computer Vision and Image Understanding*, vol. 218, p. 103407, 2022. 6, 7
- [38] X. Xie, Y. Cui, C.-I. Jeong, T. Tan, X. Zhang, X. Zheng, and Z. Yu, "Fusionmamba: Dynamic feature enhancement for multimodal image fusion with mamba," *arXiv preprint arXiv:2404.09498*, 2024. 6, 7
- [39] Y. Han, Y. Cai, Y. Cao, and X. Xu, "A new image fusion performance metric based on visual information fidelity," *Information fusion*, vol. 14, no. 2, pp. 127–135, 2013. 6
- [40] G. Cui, H. Feng, Z. Xu, Q. Li, and Y. Chen, "Detail preserved fusion of visible and infrared images using regional saliency extraction and multi-scale image decomposition," *Optics Communications*, vol. 341, pp. 199–209, 2015. 6
- [41] B. Rajalingam and R. Priya, "Hybrid multimodality medical image fusion technique for feature enhancement in medical diagnosis," *International Journal of Engineering Science Invention*, vol. 2, no. Special issue, pp. 52–60, 2018. 6
- [42] C. S. Xydeas and V. Petrovic, "Objective image fusion performance measure," *Electronics letters*, vol. 36, no. 4, pp. 308–309, 2000. 6
- [43] A. M. Eskicioglu and P. S. Fisher, "Image quality measures and their performance," *IEEE Transactions on communications*, vol. 43, no. 12, pp. 2959–2965, 1995. 6
- [44] G. Piella and H. Heijmans, "A new quality metric for image fusion," in *Proceedings 2003 international conference on image processing (Cat. No. 03CH37429)*, vol. 3. IEEE, 2003, pp. III–173. 6